

Long-Term Cycling Stability of Cobalt sulfide Nanosheets for High-Performance Magnesium-Ion Batteries

Hajra Baig, Mian Azmat, Hafiz Muhammad Naeem Ullah, Muhammad Ismail, Mingwei Jin, Muhammad Kashif Naseem, Kaung Khant Kyaw, Asif Ali, Youqi Zhu,* Chuanbao Cao,* and Meishuai Zou*

Rechargeable Magnesium ion batteries (RMIBs) are considered one of the most promising energy storage devices due to their low cost, dendrite-free nature, and ecofriendliness. However, sluggish kinetics, irreversible structural changes, short cycle life, and low capacity of cathodes hinder their practical applications. Herein, Cobalt sulfide (CoS_2) nanosheets are synthesized using microwave method followed by chemical vapor deposition to serve as cathode material for RMIBs. CoS_2 nanosheets exhibit excellent electrochemical performance, providing a high specific capacity of 432 mAh g^{-1} at 100 mA g^{-1} current density. Moreover,

CoS_2 also demonstrates a long-term operating stability over 2000 cycles giving 284 mAh g^{-1} capacity at a current density of 500 mA g^{-1} with approximately 96% capacity retention. Sustainable cathodic performance is the most desirous feature for commercialization. The density functional theory and experimental results reveal that the robust electrochemical performance of CoS_2 as a cathode is attributed to the high surface area of its sheet-like morphology. This work provides meaningful insights regarding morphological limitations and opportunities of CoS_2 cathode for applications in high-performance RMIBs.

1. Introduction

A key focus in today's modern energy industry is the development of new energy storage systems because traditional Lithium-ion (Li^+) batteries raise the major safety and economic concerns.^[1,2] Rechargeable magnesium ion batteries (RMIBs) have gained much attention as a potential replacement for Li^+ batteries in energy storage devices.^[3,4] Magnesium makes up nearly 2% of the Earth's crust, making it the eighth most common element.^[5] Previous research has shown that magnesium anodes don't greatly suffer from dendrite growth during RMIBs cycling because of their low chemical reactivity and ensures high

safety.^[6] Despite these advantages, several critical challenges hinder the practical deployment of RMIBs, chief among them being poor cycling stability. This limitation is a result of a complex interplay among different factors, e.g., strong electrostatic interactions between bivalent magnesium cations (Mg^{2+}) and the cathode materials' lattice result in sluggish solid-state ion diffusion and low storage capacity,^[7] the cathode's structural instability and strong binding of Mg^{2+} ^[8,9] with host material limit reversibility, cathode's structural framework and poor electronic conductivity influence the long-term performance and cycling.^[5] These issues collectively impact the storage capacity, Coulombic efficiency, and reversibility over extended cycling of a battery. Therefore, it's important to address the challenges related to the cathode materials to advance magnesium-ion batteries.^[10] The cathodic materials fall into two categories based on electrochemical reaction mechanisms: one is insertion-type cathodes, and the other is conversion-type cathodes. The conversion-type has an advantage over the insertion-type because the electrochemical conversion mechanism is not affected by the crystal structure, unlike the insertion mechanism.^[11–13] Therefore, conversion-type cathodes offer good cycling stability and are free from Mg^{2+} kinetic inhibition problems.

The ideal conversion-type materials are from group VI A elements, which are abundant on the Earth, like oxygen (O), sulfur (S), selenium (Se), and tellurium (Te).^[14] Among group VI A compounds, metal sulfides (MS_x) could be useful conversion-type materials for RMIBs, where the metal (M) enhances reaction kinetics during cycling, even though they have lower theoretical specific capacities than sulfur (S),^[15] which are critical for achieving long-term cycling performance. In this context, MS_x may serve as an alternative to sulfur, offering a balance between capacity and

H. Baig, M. Azmat, M. Ismail, M. Jin, M. K. Naseem, K. K. Kyaw, A. Ali, Y. Zhu, C. Cao, M. Zou
Research Center of Materials Science
Beijing Key Laboratory of Construction Tailorable Advanced Functional Materials and Green Applications
Beijing Institute of Technology
Beijing 100081, China
E-mail: yqzhu@bit.edu.cn
cbciao@bit.edu.cn
zoums@bit.edu.cn

H. M. N. Ullah
School of Science
Minzu University of China
Beijing 100081, China

C. Cao, M. Zou
Guangdong Provincial Key Laboratory of Efficient Catalysis and Energy Conversion
Beijing Institute of Technology
Zhuhai 519088, China

 Supporting information for this article is available on the WWW under <https://doi.org/10.1002/batt.202500501>

durability. There are two types of metal components used in conversion-type cathodes in RMIBs. Type I includes metals like tin (Sn), antimony (Sb), and bismuth (Bi), which combine with magnesium to produce alloys whereas Type II includes 3d transition metals that do not react with magnesium, but contribute to redox activity and structural integrity. Molybdenum disulfide (MoS_2),^[16–18] nickel disulfide (NiS_2),^[19] copper sulfide (CuS),^[20] vanadium tetra sulfide (VS_4),^[21,22] vanadium disulfide (VS_2),^[23] and cobalt sulfide (CoS)^[24] have been studied for their potential to deliver stable cycling and capacity retention in RMIBs. CoS_2 could be a promising cathode in RMIBs as it has shown a high performance for Li^+ ion batteries.^[25] Although, the addition of metal in metal sulfides (MSx) typically reduces specific capacities as compared to pure sulfur, despite sulfur's high theoretical specific capacity of 1675 mAh g^{-1} . Based on the assumed conversion of $\text{V}^0\text{-S}_4^0$ to $\text{V}^0\text{-4MgS}$, theoretical analysis indicates that VS_4 , which has a sulfur concentration of 71.6%, should have a high specific capacity. However, VS_4 has a lower actual specific capacity since it primarily serves as an intercalation material and is rarely converted to V-MgS . Although there is still limited research available on alloy-type metal sulfides such as Antimony trisulfide (Sb_2S_3), Tin sulfide (SnS_2), and Bismuth (III) sulfide (Bi_2S_3), these materials have so far demonstrated poor electrochemical performance.^[26] In addition to material selection criteria, the morphology is also an important factor and plays a crucial role in determining the long-term electrochemical performance of conversion-type cathode materials.^[27–29] The bivalent nature of Mg^{2+} ions necessitates materials with short diffusion paths and high surface area to facilitate ion transport. Nanostructuring has proven to be an effective strategy in this regard. For example, nanostructured CuS nanoparticles showed a capacity of 300 mAh g^{-1} at 100 mA g^{-1} , outperforming its bulk counterpart.^[30] 1D nanorods of WSe_2 and 2D nanosheets of CoS were preferred for reduced solid-state diffusion path of Mg^{2+} cations and better storage capacity.^[24,31] Our group also fabricated defect-rich VS_4 nanosheets, which had good cyclability and capacity retention, underscoring the importance of defect engineering and nanoscale design in achieving durable performance.^[32] According to this discussion, nanostructured conversion-type cathode materials can be a promising choice for advancing RMIBs technology.

The CoS_2 is regarded as one of the most desirable cathodes for high performance in batteries among the different conversion materials that are currently available, because of its exceptional electrical conductivity ($5 \times 10^2 \text{ S m}^{-1}$) and high theoretical capacity (871 mAh g^{-1}).^[33] However, to fully harness CoS_2 's potential for long-term cycling stability, advanced structural engineering strategies are essential. According to the previous studies, employing hollow structured micro-nanomaterials and embedding nanoscale CoS_2 particles into a shell carbon matrix are promising approaches because they can shorten the ion diffusion length, absorb or trap the polysulfide intermediates, increase electronic conductivity, accommodate strain from volume change, and prevent CoS_2 particle agglomeration, significantly enhances the material's durability and capacity retention.^[34]

The goal of this work was to develop a microwave assisted liquid phase growth of the Co(OH)_2 precursor after it had been sulfurized at room temperature in order to address the synthesis challenge of very thin CoS_x freestanding sheets (graphene-like) in an extremely quick, simple, and scalable manner.^[35] On the other hand, because of the anionic redox chemistry ($\text{S}^{2-}/\text{S}_2^{2-}$) involved, the presence of $(\text{S}_2)^{2-}$ in CoS_2 , which arises from the energy band levels close to one another between the Co 3d and S 3p orbitals, increases charge capacity.^[1] In our case, CoS_2 nanosheets achieved a high discharge capacity with long-term capacity retention and cycling stability in RMIBs.

2. Results and Discussion

The efficient and durable performance of the RMIBs originates from the morphology of the cathode materials, because morphology significantly influences the key electrochemical processes such as Mg-ion diffusion, electrolyte accessibility, and structural stability. Thus, density functional theory (DFT) calculations explored the electrochemical properties of bulk CoS_2 and its nanosheet counterpart. Theoretically optimized structure, calculated density of states (DOS), and band structure of bulk CoS_2 are shown in Figure 1. The Fermi level is set at 0 eV. The CoS_2 has pyrite structure, belongs to cubic $\text{Pa}\bar{3}$ space group, having four

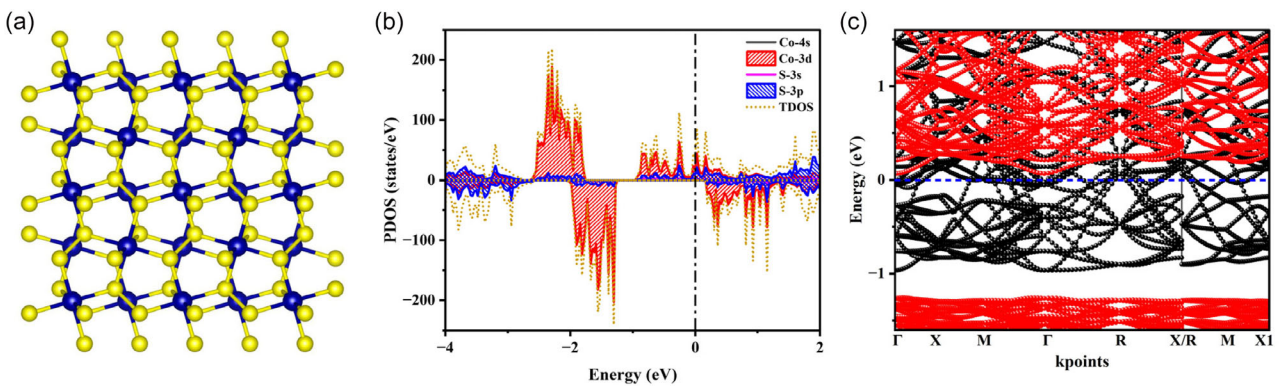


Figure 1. a) DFT-relaxed atomic structure model; b) electronic DOS plot; and c) band structure of pure CoS_2 . The yellow and blue balls indicate S and Co atoms, respectively.

formula units per unitcell, each Co atom makes an octahedral with six equivalent S atoms at the corners of the octahedral. CoS_6 octahedra share its corners with twelve equivalent CoS_6 octahedra, as well as with six equivalent SCo_3S tetrahedra. The calculated lattice constant a is 5.506 \AA which is consistant with the experimental value of 5.528 \AA .^[36] The electronic DOS and band structure plots show a metallic character of CoS_2 as the Fermi level passes through the conduction band. This enhanced conductivity can be considered a plus point to use CoS_2 as a cathode in RMBs. Figure 1b exhibits that the spin polarized valance and conduction bands are comprised of hybridized Co 3d and S 2p states. The valance band has major contribution of Co 3d states, while the conduction band has significant participation of S 2p states compared with Co 3d states. These properties agree with theoretical^[37,38] and experimental^[36,39] literature and imply that our simulation method is correct and authentic.

The Mg-ion is highly positively charged, and coulombic forces tend to keep the Mg-ion near S anions. There were two inequivalent positions in SCo_3S tetrahedral to insert Mg-ion in the CoS_2 structure. The stable position is found to intercalate Mg ions at the S-S dimer in SCo_3S tetrahedral, as shown in Figure 2a, resulting in the breaking of the S-S dimer and producing distortion in

the structure, which may affect the intercalation of Mg ions on nearby equivalent positions and hinder the diffusion of Mg ions. CoS_2 cathode showed a long activation time,^[40] and these structural distortions may be the reason behind this. To further understand the Mg ion intercalation phenomenon, charge density difference was calculated and shown in Figure 2b. Figure 2b shows the charge density difference obtained by subtracting total electron densities of CoS_2 and isolated Mg atom in the host lattice site from that of CoS_2 with intercalated Mg. The iso-value was set as 0.003 e\AA^{-3} , charge depletion was in green and accumulation in red color. It is obvious that intercalated Mg transfers its charge to nearby S atoms and breaks the S-S dimer. It is found that Mg atom is intercalated with coordination number 4 at a place having two S_2^{2-} dimers opposite to each other. However, slight charge accumulation can also be seen at nearby Co atoms. The diffusion barrier of Mg ion in bulk CoS_2 was also calculated via the nudged elastic band (NEB) method. The shortest diffusion path for Mg is the movement of Mg ion from initial position (Figure 2a) to the next nearest S-S dimer (Figure 2c). The diffusion path has been illustrated in Figure 2d. It is found that the Mg ions diffusion barrier in bulk CoS_2 is 0.63 eV , which is more than double than that of Li ion diffusion barrier of 0.26 eV in bulk CoS_2 .^[41]

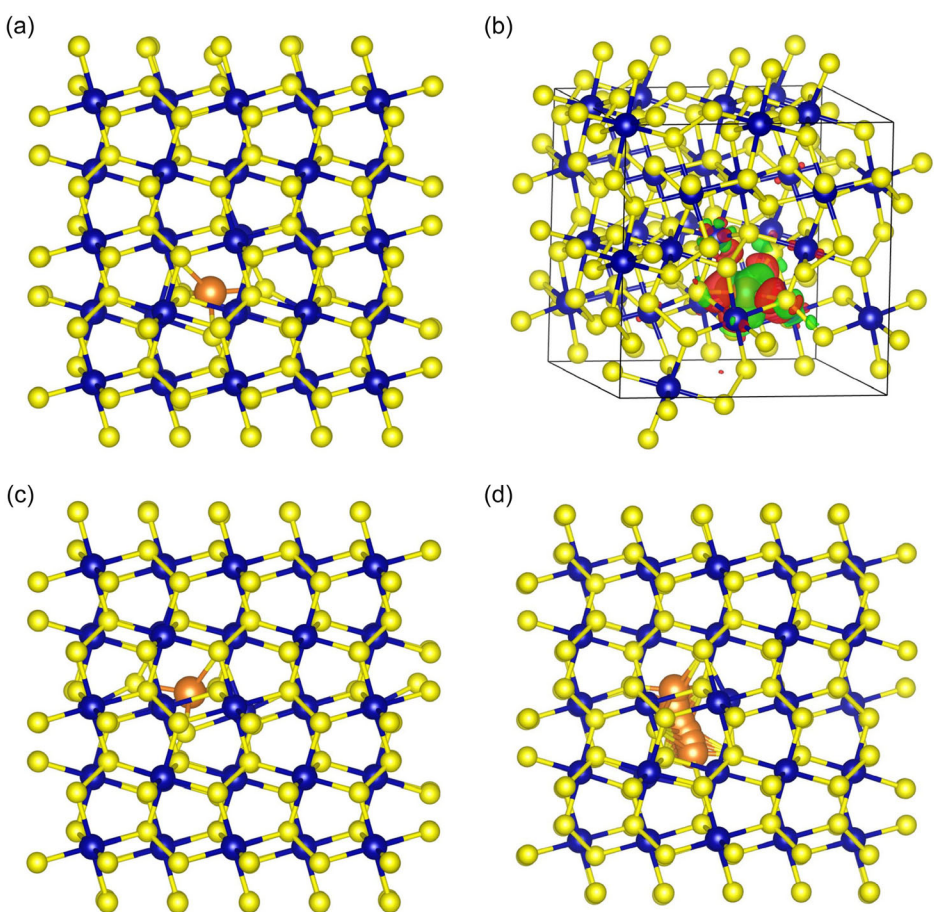


Figure 2. a,c) Initial and final positions of Mg ion intercalated at SCo_3S tetrahedral, respectively; b) charge density difference presentation of Mg-inserted CoS_2 ; and d) the NEB calculated Mg ion diffusion path in bulk CoS_2 .

indicating slower Mg-ion mobility. This elevated barrier may contribute to sluggish kinetics and capacity fading over extended cycling, especially if structural distortions accumulate.

To explore the CoS_2 surface behavior for Mg ion storage, we have simulated a CoS_2 (001) surface and calculated Mg diffusion barriers as shown in **Figure 3**. The lattice constant a is slightly reduced to 5.501 Å of the layers near surface, which becomes 5.506 Å in bulk. The Mg diffusion barrier on the surface is calculated to be 0.34 eV, while this is 0.71 eV from surface to bulk. The higher surface to bulk barrier acts as a bottleneck for Mg transport and may participate in longer activation time and reduced ion mobility over extended cycling. Since the surface Mg ion barrier is lower, optimizing the CoS_2 cathode morphology to expose more surface-active sites that can facilitate faster Mg ion transport, highlighting the importance of surface-dominated transport pathways. Furthermore, nanosized or porous structures can increase the surface area, allowing Mg ions to migrate more easily without encountering high energy, which is essential for improving long-term electrochemical stability, minimizing capacity fading, and ensuring sustained capacity retention in RMIBs.

Our aim is to increase the surface area of CoS_2 cathode to improve its performance in RMIBs. The three main approaches for creating atomic-level thin sheets are physical exfoliation,

chemical exfoliation, and high-temperature epitaxial growth. However, the first two methods are hindered by low yield and uncontrolled morphological homogeneity, whereas the latter is costly and contingent on growth.

Because of these factors, the solution-phase colloidal growth reaction is considered a capable low-cost method to produce 2D nanomaterials on a large scale.^[42,43] Therefore, we followed this method to prepare our sample. Figure S1, Supporting Information shows the schematic demonstration of the synthesis of sample. First, we prepared the Co(OH)_2 nanosheets whose structure and morphology were characterized by X-ray diffraction (XRD) and field emission scanning electron microscopy (FESEM), as shown in Figure S2, Supporting Information, as reported earlier in the literature.^[44,45] In the second step, we sulfurized the obtained nanosheets of cobalt hydroxide by chemical vapor deposition (CVD) process and got the final desired product (detailed explanation is given in experimental section) of CoS_2 nanosheets. XRD method is applied for observation of crystal phases, and the prominent peaks agree with reported data (JCPD card PDF# 41–1471) shown in **Figure 4a**, indicating a cubic phase of CoS_2 with a lattice constant of 5.538 Å.^[25,46,47] The lattice planes corresponding to the peaks are labeled in the XRD pattern. The (111) and (200) peaks of nanosheets have shifted to lower and higher

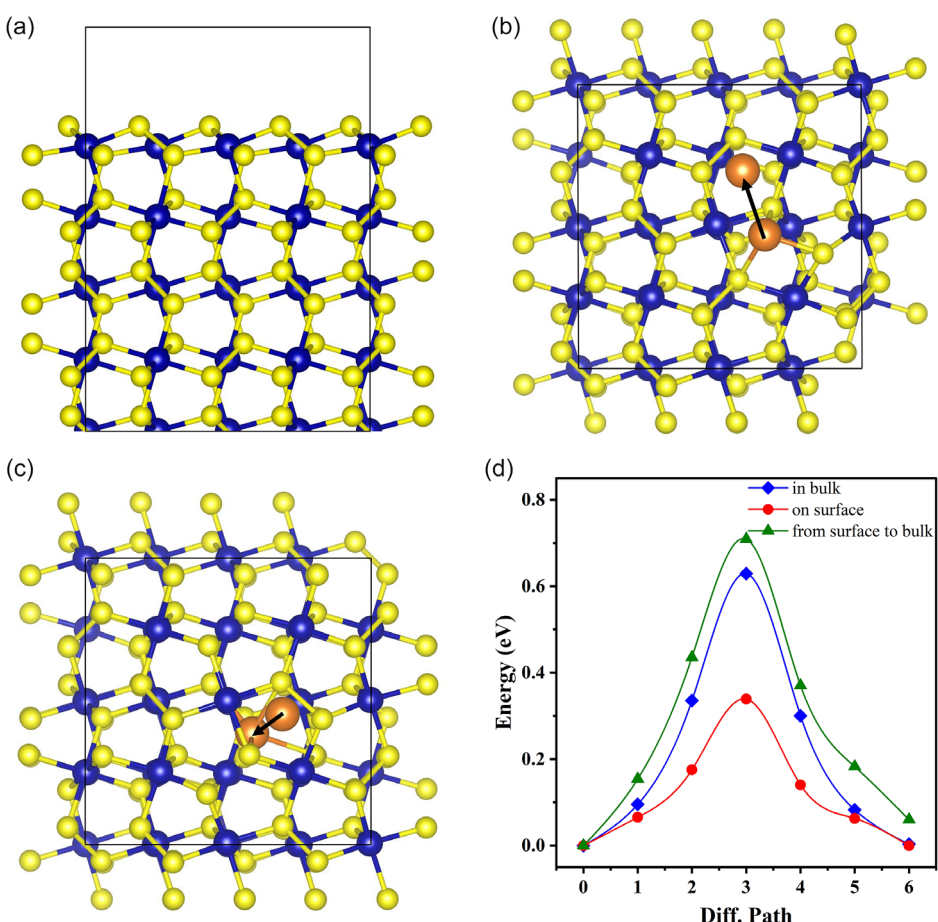


Figure 3. a) Side view of CoS_2 nanosheet DFT model with exposed (001) surface; b) the top view of Mg ion diffusion at the surface; c) from surface to bulk of CoS_2 ; and d) diffusion barriers of Mg^{2+} ion in bulk and at surface of CoS_2 .

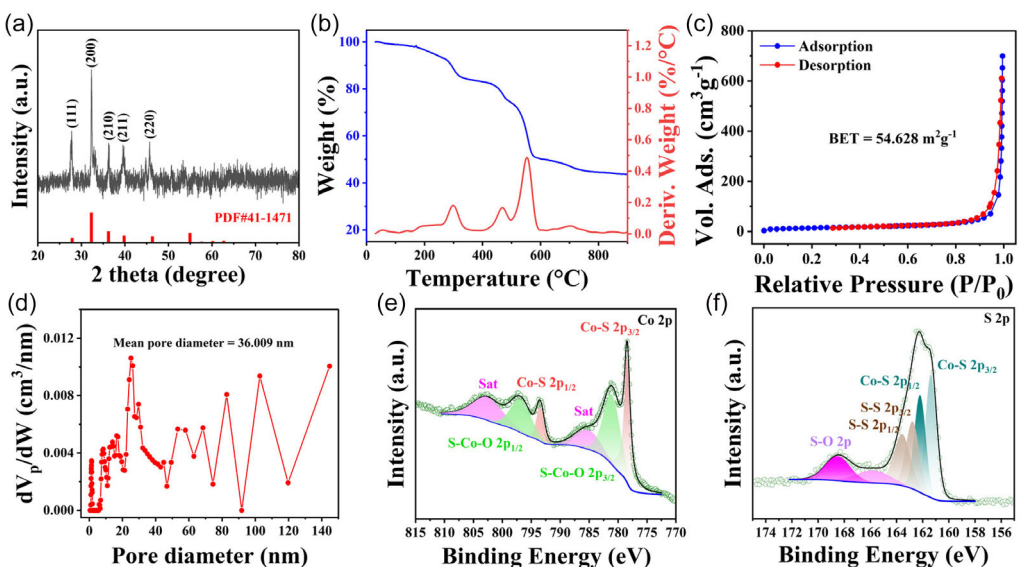


Figure 4. a) XRD patterns of CoS_2 ; b) TGA of CoS_2 ; c,d) BET and pore size of CoS_2 nanosheets; e) Co 2p; and f) S 2p XPS spectra of CoS_2 .

angles, respectively, compared to JCPD card PDF# 41–1471. This shift indicates an increase in the interplanar distance for the (111) plane and a shrinkage for the (200) plane. Thermogravimetric analysis (TGA) was performed to determine the thermal stability of CoS_2 nanosheets in Figure 4b. After TGA test in air, 43.6% material remained which means good stability with high temperature. The thermal decomposition process of CoS_2 nanosheets can be divided into three stages causing by weight loss. The first (at about 300 °C) and second (at about 470 °C) peaks of the derivative of weight for temperature can be ascribed to the dehydration and partial oxidation of CoS_2 sample surface, respectively.^[47,48] The third peak at about 552 °C is assigned to the decomposition of CoS_2 nanosheets, which is about 60 °C lower than that of crystalline CoS_2 .^[46] The N_2 adsorption/desorption tests were used to determine the porous structure of CoS_2 in Figure 4c. The Brunauer–Emmett–Teller (BET) surface area of CoS_2 nanosheets is calculated to be $54.6 \text{ m}^2 \text{ g}^{-1}$, with the pore sizes centered at ≈ 3.6 and ≈ 20 nm. This BET surface area is much larger and comparable to the surface area of defect-rich VS_4 nanosheet.^[32] This porous architecture facilitates efficient Mg ion diffusion and electrolyte access, which are critical for minimizing capacity fading and ensuring stable cycling performance. X-ray photoelectron spectroscopy (XPS) is recorded for chemical composition and valence info of CoS_2 nanosheets, which is shown in Figure 4e,f. XPS survey spectrum demonstrates the characteristic peaks of Co, S, and other present elements shown in Figure S3, Supporting Information. The spectrum of Co 2p in the CoS_2 nanosheets is shown in Figure 4e. Strong Co–S 2p_{3/2} and Co–S 2p_{1/2} peaks at 778.2 and 792.9 eV are recorded, resulting in the main valence state of Co as Co^{2+} .^[49] Two distinct satellite peaks for Co–S 2p_{3/2} and Co–S 2p_{1/2} at 786.5 and 802.8 eV are also observed.^[50]

By exposure to the environment, surface oxidation happened, and two peaks observed at 781.3 and 797.5 eV are attributed to S–Co–O bond.^[51,52] S 2p XPS spectrum is shown in Figure 4f. Two sharp peaks deconvoluted at 161.5 and 162.3 eV represent S–Co

2p_{3/2} and 2p_{1/2}, respectively.^[53] In addition, two peaks at 163.2 and 164.5 eV indicate the S–S bond of the bridging S_2^{2-} in CoS_2 .^[54] Another two peaks located at 168.5 and 169.6 eV are assigned to S–O bond due to surface oxidation.^[55]

The morphological and microstructural information of CoS_2 nanosheets were analyzed by scanning electron microscope (SEM) and high-resolution transmission electron microscope (HRTEM), as shown in Figure 5a–f. It is observed from SEM images given in Figure 5a–c that the prepared CoS_2 nanosheets exhibit large planar area and are stacked on each other, resembling graphene sheets. However, these CoS_2 nanosheets do not form a hierarchical closed 3D structure. This open morphology is advantageous for ion transport and electrolyte accessibility. HRTEM images depicted in Figure 5d–f reveal that formed nanosheets are ultrathin with large surface area; this observation is consistent with SEM results. A greater surface area of CoS_2 ultrathin nanosheets can provide more active sites for electrochemical reactions, improving the charge and discharge rates of RMIBs, which can contribute to improved rate capability and capacity retention in RMIBs. Figure 5f shows interplanar spacing of 0.266 and 0.328 nm corresponding to (200) and (111) planes, while these distances are 0.276 and 0.318 nm for bulk CoS_2 . It means the (200) lattice spacing shrinks while (111) expands in nanosheets. These results agree with XRD findings. Figure 5g–i presents the energy-dispersive X-ray spectroscopy (EDS) elemental mapping, in which Co and S are uniformly distributed in the nanosheets and no segregation of any element detected.

To understand the electrochemical properties of CoS_2 nanosheets, the Cyclic Voltammetry (CV) of an activated cell was recorded to quantify the magnesium storage through galvanostatic charging–discharging process at 0.1 mV s^{-1} in the voltage window 0.1–2.1 V shown in Figure 6a. We observed clear reduction peak at 0.98 V and three other small peaks at 0.45, 1.53, and 1.99 V. The cathode peak at 0.98 V confirms the magnisiation of CoS_2 nanosheets producing MgS intermediates, while reduction

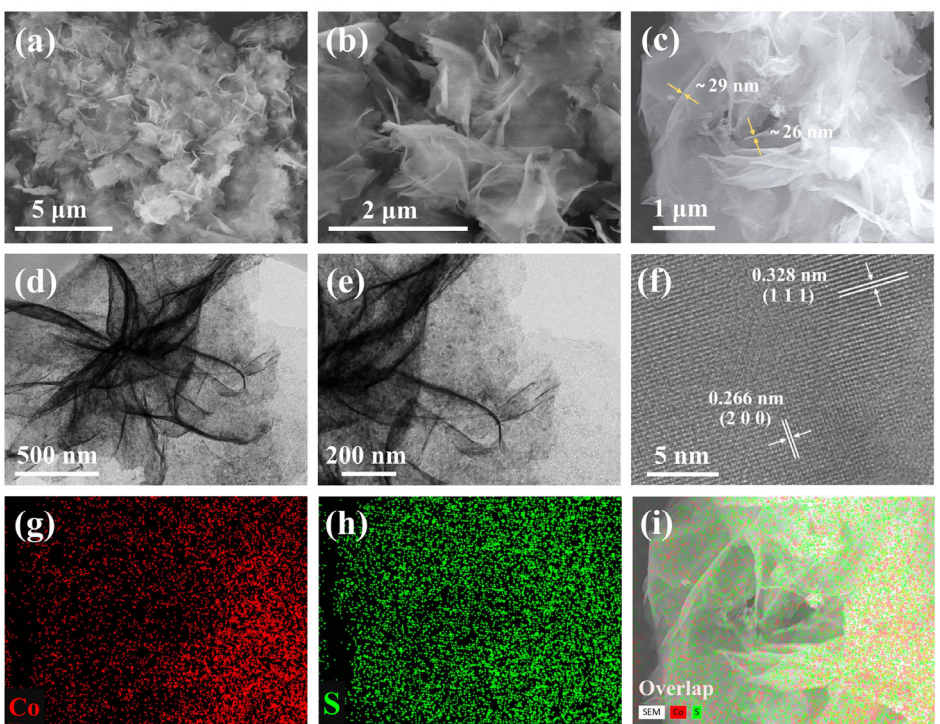


Figure 5. SEM imagery a,b) at low magnification; c) at high magnification; d,e) transmission electron microscopy (TEM) images; f) HRTEM image displaying d-spacing; and g-i) element distribution mappings of Co, S, and CoS_2 respectively.

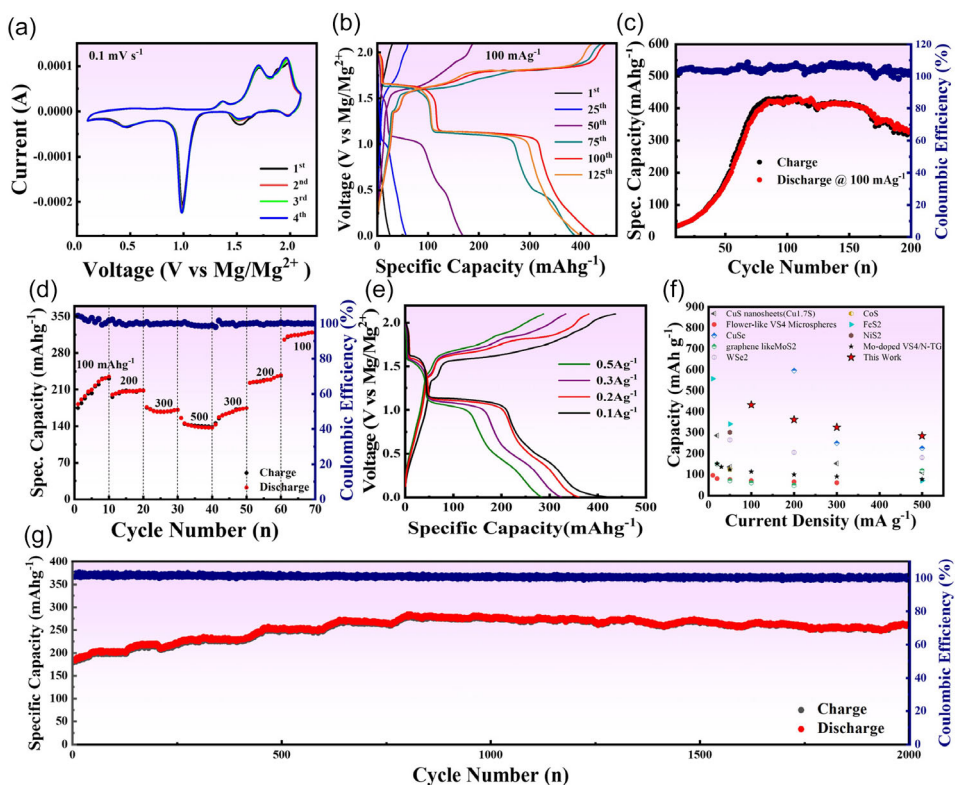


Figure 6. a) CV at scan rate 0.1 mV s^{-1} ; b) galvanostatic charge–discharge cycling performance at 100 mA g^{-1} ; c) charging–discharging curves at 100 mA g^{-1} ; d) step performance; e) charging–discharging curves of the best-performing cycles at different current rates, illustrating the electrochemical performance and rate capability of RMIBs; f) comparison of this work with other recently published; and g) cycling performance of CoS_2 at 500 mA g^{-1} .

peaks at 0.5 and 1.99 V can be ascribed to Cu side reactions and 1.5 V peak can be assigned to the insertion of Mg^{2+} into the CoS_2 electrode of Cu current collector. Oxidation peaks can be seen at 1.75 and 1.97 V along with a weak peak at 1.46 V. The oxidation peak at 1.75 indicates demagnisiation of CoS_2 and conversion of S^{2-} to S_2^{2-} , while the oxidation peaks at 1.46 and 1.97 V are indicative of the transformation of Cu^{+} to Cu^{2+} and Cu to Cu^{2+} , respectively.^[32,56] All the cycles have homogenously followed each other, demonstrating excellent reversibility. This suggests that nanosheets can significantly enhance electrochemical performance, providing a higher specific capacity due to their large surface area. The galvanostatic charge–discharge curves of CoS_2 nanosheets under a current density of 100 mA g^{-1} are displayed in Figure 6b. During the initial cycles, the charge/discharge plateaus are not well-defined but become increasingly prominent and stable by the 75th cycle, suggesting a gradual but efficient activation process. However, the activation time is shorter compared to commercially available CoS_2 using the same PMC electrolyte (Figure S4, Supporting Information). The main characteristics of the charge–discharge profiles align well with the CV curves, highlighting their consistency and reinforcing the electrochemical behavior of the system. Figure 6c provides the short-term cycling characteristics of CoS_2 nanosheet cathode. The highest discharging capacity observed is 432 mAh g^{-1} at 109th cycle which is rather higher than other pristine materials.^[13,31,57] Such excellent storage performance may be attributed to the fact that CoS_2 nanosheets provide efficient ion transport, having smaller Mg^{2+} barrier on the surface as discussed in the theoretical study, and large porous surface area serves as plentiful active sites (as shown in BET graph and HRTEM photographs), facilitating the anchoring of Mg^{2+} ions. Figure 6d shows the rate performance of an inactivated cell. The discharge specific capacity varies across different current densities, the average discharge capacities are 209.8 , 206 , 171.1 , 139.3 , 167.7 , 228.6 , and 315.3 mAh g^{-1} at 0.1 , 0.2 , 0.3 , 0.5 , 0.3 , 0.2 , and 0.1 A g^{-1} , respectively. This data highlights the CoS_2 nanosheets' performance across a broad range of operating conditions. Figure 6e presents the typical charge–discharge voltage profiles of CoS_2 nanosheets, exhibiting a consistent shape with an extended and stable voltage platform. These characteristics render excellent electrochemical reaction kinetics. Furthermore, the CoS_2 nanosheets' electrochemical performance has been compared to other recently reported cathode materials for RMIBs and demonstrates superior performance (Figure 6f). The long-life cyclic stability of the CoS_2 nanosheets at a current density of 0.5 A g^{-1} is illustrated in Figure 6g. The maximum discharge capacity of 284.3 mAh g^{-1} is noticed, which remains stable over 2000 cycles with a minimal capacity decay. The discharge capacity was 272 mAh g^{-1} at the end of 2000 cycles. This outstanding cyclic durability, combined with shortened activation time, underscores the nanosheets' potential for high-performance, long-life Mg-ion battery applications.

To further understand the electrochemical kinetics of CoS_2 nanosheets and their implications for long-term Mg-ion battery performance, Figure 7a displays CV profiles of CoS_2 nanosheets over different scan rates from 0.1 to 1.0 mV s^{-1} between the

potential window of 0.1 – 2.1 V . All CV profiles maintain identical shapes, signifying stable electrochemical properties and strong rate capability. The cathodic peaks (P_c and P_d) potential falls gradually, and the anodic peaks (P_a and P_b) potential rises with the increase in scan rate, indicating the effect of enhanced polarization under high load conditions. To further analyze kinetic reaction, we used the power law formula $i = av^b$, where i and v are current and scan rate, respectively, and a and b are empirical parameters. So, the equation representing kinetic reaction type can be written as

$$\log(i) = b \log(v) + \log(a) \quad (1)$$

When the value of b is ≈ 0.5 , the electrochemical process is primarily diffusion-controlled. However, as b approaches 1.0 , the electrochemical behavior is predominantly pseudocapacitive.^[32] Obtaining peak current values from CV curves and calculating the b values by plotting $\log(i)$ and $\log(v)$ (Figure 7b) suggest that CoS_2 nanosheets have diffusion-dominant reaction kinetics. The following equation is used to quantify the percentage contribution of diffusion and capacitive processes^[32]

$$i = k_1 v + k_2 v^{1/2} \quad (2)$$

where k_1 and k_2 are proportionality coefficients. The calculated ratios are plotted in Figure 7c, where the diffusion contribution of pristine CoS_2 is 95.62 , 91.612 , 88.54 , and 87.35% at 0.1 , 0.4 , 0.8 , and 1.0 mV s^{-1} scan rate, respectively. This indicates that CoS_2 nanosheets have highly diffusive capability attributed to the abundance of active sites due to nanosheets' high surface area, reduced Mg^{2+} diffusion barrier, and shortened ion transport pathways, all of which may contribute to enhanced ion accessibility and stable electrochemical performance over extended cycling. Furthermore, R^2 value of CoS_2 cathode from the linear fitting in Figure 7d is very close to 1 , indicating the excellent reversibility of CoS_2 cathode, a critical factor for long-term capacity retention.

The magnesium storage behavior of CoS_2 nanosheets was investigated through ex situ XPS analysis, Figure 8 displays ex situ high-resolution XPS spectra of CoS_2 nanosheet cathodes at different discharge stages. The pristine $Co 2p_{3/2}$ peak at 778.2 eV slightly shifts to higher binding energy upon discharging, while the strong satellite peaks attributed to ligand-to-metal charge transfer remain distinct. This indicates that cobalt maintains its $+2$ oxidation state throughout the charge–discharge cycle. During the discharge process, the insertion of Mg^{2+} ions causes the pristine $S 2p$ peaks at 161.5 and 162.3 eV shift to lower binding energy, while the intensity of peaks at 163.2 and 164.5 eV , assigned to S_2^{2-} dimers, reduces and this effect is maximum when the battery is fully discharged shown in Figure 8c. Additionally, the $Mg 2p$ peak at 49.9 eV appears in both partially and fully discharged cells (Figure S5, Supporting Information), confirming that oxidation state of Mg is $+2$.^[58] This phenomenon results from Mg–S interactions, indicating the conversion reaction by breaking of S_2^{2-} dimers into S^{2-} . These ex situ XPS findings are consistent with DFT calculations that Mg preferentially attaches at the S–S dimer sites on the CoS_2 surface, transferring its two electrons to the two S_2^{2-} anions of the S–S dimer during

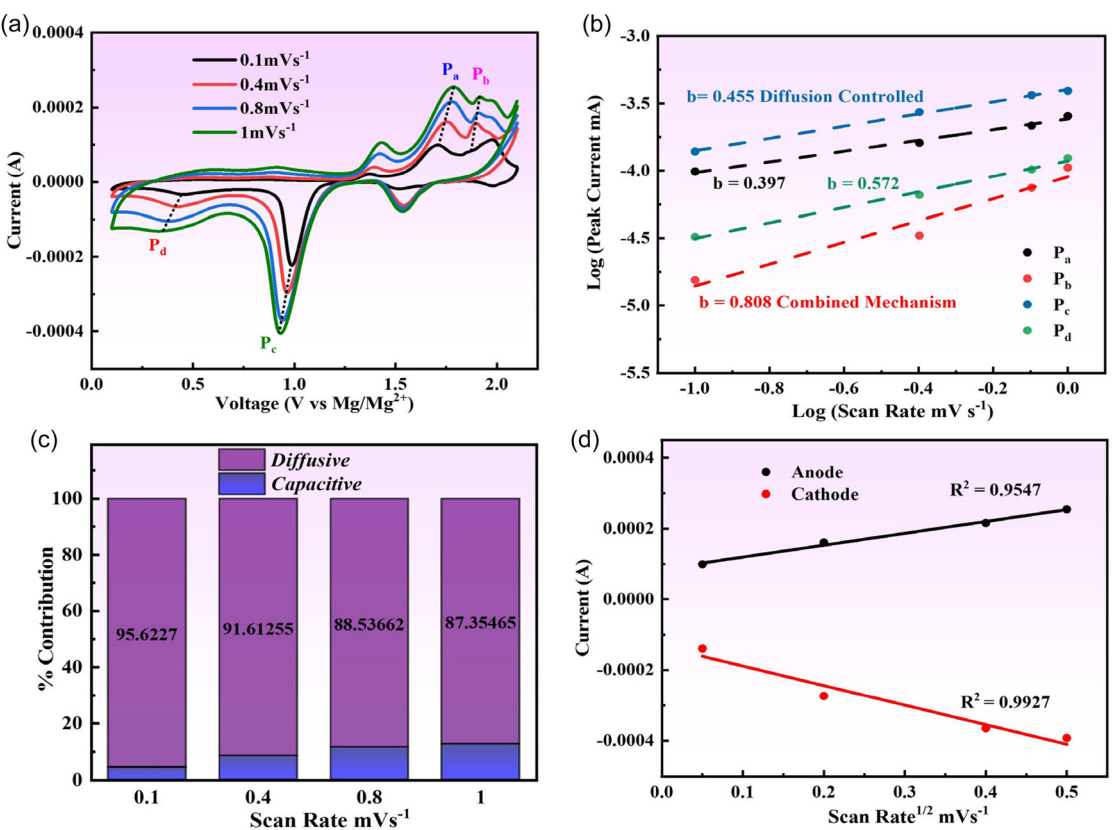


Figure 7. a) Electrochemical reaction kinetics CV curves from scan rate 0.1 mVs^{-1} to 1 mVs^{-1} ; b) b value analysis graph; c) diffusive and capacitive relation; and d) linear relationship plot between current and square root of scan rate of CoS₂.

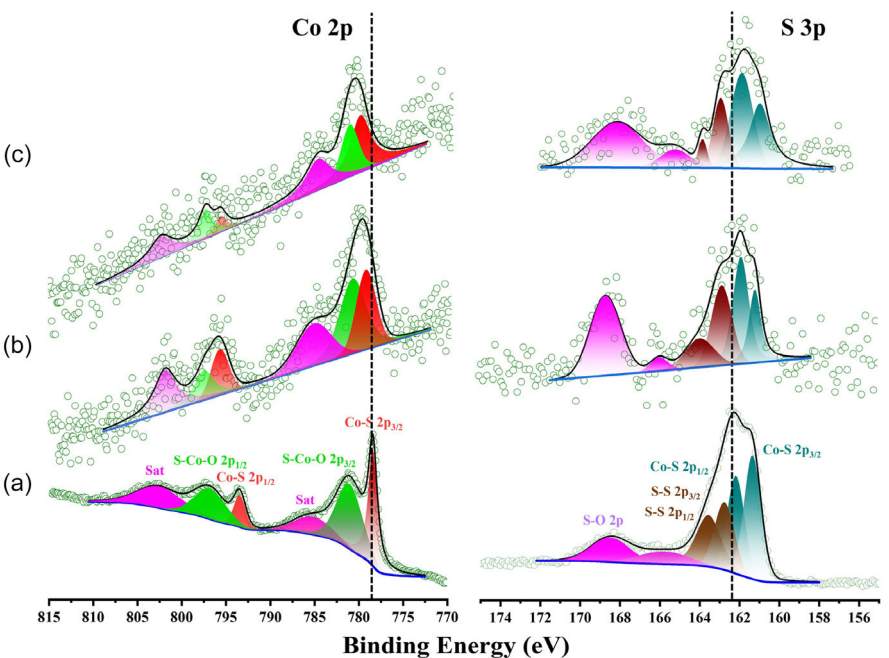


Figure 8. Ex situ high-resolution XPS spectra of Co 2p and S 2p at different discharge states. a) Pristine state before discharge; b) discharged to 1.0 V; and c) completely discharged.

conversion reaction. Consequently, the S_2^{2-} anions are converted into S^{2-} anions, leading to the formation of Mg–S bonds. This mechanism allows for storage of Mg^{2+} ions in CoS_2 structure, following the overall reaction described as; $xMg^{2+} + 2xe^- + CoS_2[S_2^{2-}] \rightarrow xMgCoS_2[S^{2-}]$. Together with the reversible S–S bond transformation and stable Mg–S interactions, the preservation of Co's oxidation state highlights the ability of CoS_2 nanosheets to retain electrochemical activity and structural integrity at long-term use.

3. Conclusion

In summary, the theoretical and experimental investigations conclusively demonstrate that the nanosheet morphology of CoS_2 cathode enhances the electrochemical performance of Mg-ion batteries. The DFT calculations reveal a significantly lower Mg^{2+} diffusion barrier of 0.34 eV on the CoS_2 nanosheet surface compared to 0.63 eV in bulk CoS_2 , rationalizing the accelerated ion kinetics and reduced activation energy. Through theoretical calculations, it is found that structural changes in bulk CoS_2 and higher surface to bulk Mg^{2+} diffusion barrier (0.71 eV) lead to longer activation time and lower Mg^{2+} storage capacity. By synthesizing ultrathin CoS_2 nanosheets via two step microwave-assisted CVD approach, we achieved an excellent capacity of 432 mAh g⁻¹ at 100 mA g⁻¹ and outstanding long-term cyclability, exhibiting capacity of 284 mAh g⁻¹ at 500 mA g⁻¹ with almost 96% retention after 2000 cycles. The nanosheet architecture shortens Mg^{2+} diffusion pathways on the one hand and ensures structural resilience against repeated cycling, mitigating degradation on the other hand. This study highlights the critical role of morphological engineering in optimizing CoS_2 cathodes for high-performance rechargeable Mg-ion batteries, offering a scalable strategy to address kinetic limitations and stability challenges in multivalent ion storage systems.

4. Experimental Section

Material Synthesis

Cobalt sulfide (CoS_2) is synthesized in two steps. In the first step, we prepared cobalt hydroxide nanosheets $Co(OH)_2$. As per earlier findings, incredibly thin unsupported nanosheets were produced using an easy microwave-assisted approach.^[59,60] According to the conventional method, 10 mmol of Cobalt nitrate hexahydrate ($Co(NO_3)_2 \cdot 6H_2O$) and 15 mmol of urea was dissolved in a mixture of deionized water (10 ml) and ethylene glycol (60 ml) for 30 min to get a pink homogenous solution. Then this solution was put into the microwave for 30 min at 150 °C and 500 W. A bulbous, dark purple colloidal solution was obtained. We washed it several times with water and ethanol sequentially. The final precipitate was put into the drying oven at 80 °C for overnight. In the second step, we obtained extremely thin free nanosheets of cobalt hydroxide and sublime sulfur with 1:5 and put them in the CVD at 350 °C for 4 h in an inert gas (argon) atmosphere. Subsequently, the product was retrieved upon its cooling to ambient temperature.

Electrochemical Measurements

A homogenous slurry constituted with 80% activated material, 10% Carbon black, and 10% polyvinylidene difluoride (PVDF) in N-methylene-2-pyrrolidone (NMP) as solvent was prepared. Then prepared slurry is coated on the copper sheet and dried in oven for 6 h, then we cut it into 14 mm diameter discs and use them as working electrodes. Then coin cells consisting of prepared working electrode, a separator (Whatman microfiber glass paper), Mg metal anode, and non-nucleophilic PMC electrolyte i.e., [(R-PhOMgCl)₂-AlCl₃/THF, where R is the alkyl group of 2-tert-butyl 4-methylphenol] (preparation of electrolyte is given in Supporting Information.) were assembled in glove box filled with argon gas ($H_2O < 0.1$, $O_2 < 1$ ppm). The method of preparing electrolyte is given in supporting information. Galvanostatic charging and discharging test of prepared cells were recorded on CT2001A LAND battery test system. CV measurements were executed with electrochemical station (CHI 760E).

Computational Details

All DFT calculations were performed using the Vienna Ab initio Simulation Package (VASP). The study focused on the structural and electronic properties of CoS_2 . The projector-augmented wave (PAW) method was used for core electrons^[61] and the generalized gradient approximation (GGA) with Perdew–Burke–Ernzerhof (PBE) exchange–correlation functional handled valence electrons.^[62,63] Valence electron configurations for Co, S, and Mg were considered as $3p^63d^74s^2$, $3s^23p^4$, and $2s^22p^63s^1$, respectively. Spin polarization was considered in all calculations. The calculations utilized uniform Monkhorst–Pack k-points grids of $4 \times 4 \times 4$ and $4 \times 4 \times 2$ for Brillouin zone sampling during structural optimization and electronic calculations of bulk CoS_2 and its nanosheet counterpart, respectively. A plane-wave basis set with a cutoff energy of 500 eV ensured accurate results, with energy and force convergence thresholds set at 10 eV and 0.01 eV Å⁻¹, respectively. The vacuum space of 20 Å was set between periodic images of CoS_2 nanosheets to avoid any interaction between the nanosheet and its periodic images.

Acknowledgements

The authors acknowledge the financial support from the National Natural Science Foundation of China (21371023 and 52173273).

Conflict of Interest

The authors declare no conflict of interest.

Author Contributions

Hajra Baig: conceptualization (lead); investigation (lead); writing—original draft; (lead). **Mian Azmat:** software (equal). **Hafiz Muhammad Naeem Ullah:** software (equal). **Muhammad Ismail:** data curation (supporting). **Mingwei Jin:** data curation (supporting). **Muhammad Kashif Naseem:** data curation (supporting). **Kaung Khant Kyaw:** data curation (supporting). **Asif Ali:** data curation (supporting). **Youqi Zhu:** writing—review & editing (equal). **Chuanbao Cao:** writing—review & editing (lead). **Meishuai Zou:** writing—review & editing (equal).

Data Availability Statement

The data that support the findings of this study are available in the supplementary material of this article.

Keywords: cobalt disulfide · nanosheets · promising cathode · rechargeable magnesium ion battery

- [1] R. Zhuang, Z. Huang, S. Wang, J. Qiao, J. C. Wu, J. Yang, *Chem. Eng. J.* **2021**, 409, 128235.
- [2] Y. Zhang, H. Geng, W. Wei, J. Ma, L. Chen, C. C. Li, *Energy Storage Mater.* **2019**, 20, 118.
- [3] J. Zhang, Z. Chang, Z. Zhang, A. Du, S. Dong, Z. Li, G. Li, G. Cui, *ACS Nano* **2021**, 15, 15594.
- [4] S. Wang, X. Zhao, *Energy Fuels* **2023**, 37, 18441.
- [5] M. Mao, T. Gao, S. Hou, C. Wang, *Chem. Soc. Rev.* **2018**, 47, 8804.
- [6] Y. Wang, H. Huang, G. Jia, H. Zeng, G. Yuan, *Acta Biomater.* **2021**, 135, 705.
- [7] H. Xu, X. Zhang, T. Xie, Z. Li, F. Sun, N. Zhang, H. Chen, Y. Zhu, X. Zou, C. Lu, J. Zou, R. M. Laine, *Energy Storage Mater.* **2022**, 46, 583.
- [8] Y. Li, Y. Zheng, K. Guo, J. Zhao, C. Li, *Energy Mater. Adv.* **2022**, 2022, <https://spj.science.org/doi/full/10.34133/2022/9840837>.
- [9] Y. Shen, Q. Zhang, Y. Wang, L. Gu, X. Zhao, X. Shen, *Adv. Mater.* **2021**, 33, 2103881.
- [10] H. D. Yoo, I. Shterenberg, Y. Gofer, G. Gershinsky, N. Pour, D. Aurbach, *Energy Environ. Sci.* **2013**, 6, 2265.
- [11] Z. Zhang, S. Dong, Z. Cui, A. Du, G. Li, G. Cui, *Small Methods* **2018**, 2, 1800020.
- [12] R. Zhang, C. Ling, F. Mizuno, *Chem. Commun.* **2015**, 51, 1487.
- [13] Z. Chen, Z. Zhang, A. Du, Y. Zhang, M. Men, G. Li, G. Cui, *Chem. Commun.* **2019**, 55, 4431.
- [14] H. Xu, D. Zhu, W. Zhu, F. Sun, J. Zou, R. M. Laine, W. Ding, *Chem. Eng. J.* **2022**, 428, 131031.
- [15] Y. Cao, Y. Zhu, C. Du, X. Yang, T. Xia, X. Ma, C. Cao, *ACS Nano* **2022**, 16, 1578.
- [16] F. Zhu, H. Zhang, Z. Lu, D. Kang, L. Han, *J. Energy Storage* **2021**, 42, 103046.
- [17] C. Zhang, A. Xu, S. Mao, Z. Li, J. Yan, F. Jiang, Y. Wang, K. Zhang, Y. Zhou, *J. Alloys Compd.* **2025**, 1010, 177309.
- [18] A. Xu, Y. Liu, J. Wang, Y. Wang, F. Jiang, Y. Zhou, *Inorg. Chem. Front.* **2024**, 11, 7831.
- [19] J. Wang, A. D. Handoko, Y. Bai, G. Yang, Y. Li, Z. Xing, M. F. Ng, Z. W. Seh, *Nano Lett.* **2022**, 22, 10184.
- [20] J. Shen, Y. Zhang, D. Chen, X. Li, Z. Chen, S. A. Cao, T. Li, F. Xu, *J. Mater. Chem. A* **2019**, 7, 21410.
- [21] Z. Li, S. Ding, J. Yin, M. Zhang, C. Sun, A. Meng, *J. Power Sources* **2020**, 451, 227815.
- [22] M. K. Naseem, M. Azmat, C. Du, R. Jiang, Hajra, Y. Zhu, M. Zou, C. Cao, *J. Mater. Chem. A* **2023**, 11, 24878.
- [23] R. Sun, C. Pei, J. Sheng, D. Wang, L. Wu, S. Liu, Q. An, L. Mai, *Energy Storage Mater.* **2018**, 12, 61.
- [24] D. He, D. Wu, J. Gao, X. Wu, X. Zeng, W. Ding, *J. Power Sources* **2015**, 294, 643.
- [25] L. Sun, X. Bao, Y. Li, J. Zhao, P. Chen, H. Liu, X. Wang, W. Liu, *Acs Appl. Nano Mater.* **2023**, 6, 11095.
- [26] S. Dey, J. Lee, S. Britto, J. M. Stratford, E. N. Keyzer, M. T. Dunstan, G. Cibin, S. J. Cassidy, M. Elgaml, C. P. Grey, *J. Am. Chem. Soc.* **2020**, 142, 19588.
- [27] X. Liu, Y. Zhu, C. Du, J. Tian, L. Yang, X. Yao, Z. Wang, X. Ma, J. Hou, C. Cao, *Chem. Eng. J.* **2023**, 463, 142433.
- [28] X. Liu, Q. Zhang, C. Du, X. Du, Y. Zhu, C. Cao, *Mater. Chem. Front.* **2023**, 7, 4400.
- [29] Z. Wang, Y. Zhang, H. Peng, C. Du, Z. Han, X. Ma, Y. Zhu, C. Cao, *Electrochim. Acta* **2022**, 407, 139786.
- [30] K. V. Kravchyk, R. Widmer, R. Erni, R. J. C. Dubey, F. Krumeich, M. V. Kovalenko, M. I. Bodnarchuk, *Sci. Rep.* **2019**, 9, 7988.
- [31] B. Liu, T. Luo, G. Mu, X. Wang, D. Chen, G. Shen, *ACS Nano* **2013**, 7, 8051.
- [32] R. Jiang, B. Liu, C. Du, M. Jin, X. Liu, X. Ma, Y. Zhu, M. Zou, C. Cao, *Chem. Eng. J.* **2024**, 488, 150487.
- [33] Y. Ma, Y. Ma, D. Bresser, Y. Ji, D. Geiger, U. Kaiser, C. Streb, A. Varzi, S. Passerini, *ACS Nano* **2018**, 12, 7220.
- [34] F. Han, C. Zhang, B. Sun, W. Tang, J. Yang, X. Li, *Carbon* **2017**, 118, 731.
- [35] R. Souleymen, Z. Wang, C. Qiao, M. Naveed, C. Cao, *J. Mater. Chem.* **2018**, 6, 7592.
- [36] E. Nowack, D. Schwarzenbach, T. Hahn, *Acta Crystallogr., Sect. B: Struct. Sci.* **1991**, 47, 650.
- [37] Z. Y. Feng, Y. Yang, J. M. Zhang, *Solid State Commun.* **2018**, 273, 60.
- [38] Y. L. Zhu, C. J. Wang, F. Gao, Z. X. Xiao, P. L. Zhao, J. Y. Wang, *R. Soc. Open Sci.* **2020**, 7, 191653.
- [39] N. Wu, Y. B. Losovoj, D. Wisbey, K. Belashchenko, M. Manno, L. Wang, C. Leighton, P. A. Dowben, *J. Phys.: Condens. Matter* **2007**, 19, 156224.
- [40] H. Xu, Y. Li, D. Zhu, Z. Li, F. Sun, W. Zhu, Y. Chen, J. Zhang, L. Ren, S. Zhang, J. Zou, R. M. Laine, *Adv. Energy Mater.* **2022**, 12, 2201608.
- [41] S. Jing, C. Zhao, X. Zhang, S. Kong, X. Lan, Z. Ma, H. Feng, W. Gong, K. Tian, Q. Li, Y. Feng, *Adv. Mater. Interfaces* **2022**, 9, 2201230.
- [42] Y. Zhu, T. Cao, C. Cao, X. Ma, X. Xu, Y. Li, *Nano Res.* **2018**, 11, 3088.
- [43] C. Tan, X. Cao, X. J. Wu, Q. He, J. Yang, X. Zhang, J. Chen, W. Zhao, S. Han, G. H. Nam, M. Sindoro, H. Zhang, *Chem. Rev.* **2017**, 117, 6225.
- [44] Y. Zhu, C. Cao, S. Tao, W. Chu, Z. Wu, Y. Li, *Sci. Rep.* **2014**, 4, 5787.
- [45] C. Qiao, Y. Zhang, Y. Zhu, C. Cao, X. Bao, J. Xu, *J. Mater. Chem. A* **2015**, 3, 6878.
- [46] S. Xie, Y. Deng, J. Mei, Z. Yang, W. M. Lau, H. Liu, *Electrochim. Acta* **2017**, 231, 287.
- [47] Y. Ji, X. Liu, W. Liu, Y. Wang, H. Zhang, M. Yang, X. Wang, X. Zhao, S. Feng, *RSC Adv.* **2014**, 4, 50220.
- [48] E. Tomaszewicz, M. Kotfica, *J. Therm. Anal. Calorim.* **2003**, 74, 583.
- [49] D. C. Higgins, F. M. Hassan, M. H. Seo, J. Y. Choi, M. A. Hoque, D. U. Lee, Z. Chen, *J. Mater. Chem. A* **2015**, 3, 6340.
- [50] N. Yao, T. Tan, F. Yang, G. Cheng, W. Luo, *Mater. Chem. Front.* **2018**, 2, 1732.
- [51] P. Chen, T. Zhou, M. Chen, Y. Tong, N. Zhang, X. Peng, W. Chu, X. Wu, C. Wu, Y. Xie, *Acs Catal.* **2017**, 7, 7405.
- [52] Y. Lin, Z. Qiu, D. Li, S. Ullah, Y. Hai, H. Xin, W. Liao, B. Yang, H. Fan, J. Xu, C. Zhu, *Energy Storage Mater.* **2018**, 11, 67.
- [53] J. Xie, S. Liu, G. Cao, T. Zhu, X. Zhao, *Nano Energy* **2013**, 2, 49.
- [54] Y. Liu, J. Zhang, S. Wang, K. Wang, Z. Chen, Q. Xu, *New J. Chem.* **2014**, 38, 4045.
- [55] C. Xu, Y. Jing, J. He, K. Zhou, Y. Chen, Q. Li, J. Lin, W. Zhang, *J. Alloys Compd.* **2017**, 708, 1178.
- [56] Z. Li, Y. Li, Y. Zhan, X. Lin, Y. Yao, T. Zhao, F. Sun, H. Xu, Z. Ma, W. Zhang, Y. Xue, X. Li, A. Vlad, J. Zou, *Angew. Chem., Int. Ed.* **2025**, 64, e202416960.
- [57] Y. Tian, J. Chen, G. Wang, B. Sun, A. Meng, L. Wang, G. Li, J. Huang, S. Ding, Z. Li, *J. Energy Chem.* **2024**, 89, 89.
- [58] N. Jäggi, C. A. Dukes, *Surf. Sci. Spectra* **2025**, 32, 014001.
- [59] Y. Zhu, C. Cao, S. Tao, W. Chu, Z. Wu, Y. Li, *Sci. Rep.* **2014**, 4, 5787.
- [60] Y. Zhu, C. Cao, J. Zhang, X. Xu, *J. Mater. Chem. A* **2015**, 3, 9556.
- [61] M. Azmat, J. Yang, H. Jin, Hajra, S. Shoaib, M. K. Naseem, Q. Li, J. Li, *Acs Appl. Opt. Mater.* **2024**, 2, 350.
- [62] M. Azmat, J. Yang, Q. Li, J. Zhang, J. Haibo, N. M. Kashif, J. Li, *Ceram. Int.* **2024**, 50, 11119.
- [63] M. Azmat, J. Haibo, K. Naseem, C. Ling, J. Li, *J. Phys. Chem. Solids* **2023**, 180, 111439.

Manuscript received: July 1, 2025

Revised manuscript received: August 17, 2025

Version of record online: